Universiteit Leiden
The Netherlands

ALMA observations of supernova remnant N49 in the large magellanic cloud. II. non-LTE analysis of shock-heated molecular clouds

Sano, H.; Yamane, Y.; Loon, J.T. van; Furuya, K.; Fukui, Y.; Alsaberi, R.Z.E.; ... ; Tachihara, K.

Note: To cite this publication please use the final published version (if applicable).

CrossMark

ALMA Observations of Supernova Remnant N49 in the Large Magellanic Cloud. II. Non-LTE Analysis of Shock-heated Molecular Clouds

H. Sano[1,2] , Y. Yamane[3] , J. Th. van Loon[4] , K. Furuya[5] , Y. Fukui[3] , R. Z. E. Alsaberi[6] , A. Bamba[7,8,9] ,
R. Enokiya[1,5] , M. D. Filipović[6] , R. Indebetouw[10,11] , T. Inoue[12] , A. Kawamura[5] , M. Lakićević[13] , C. J. Law[10,14] ,
N. Mizuno[5], T. Murase[1] , T. Onishi[15], S. Park[16] , P. P. Plucinsky[14] , J. Rho[17] , A. M. S. Richards[18] , G. Rowell[19] ,
M. Sasaki[20] , J. Seok[21,22] , P. Sharda[23] , L. Staveley-Smith[24,25] , H. Suzuki[12] , T. Temim[26] , K. Tokuda[5,27] ,
K. Tsuge[7] , and K. Tachihara[3]

[1] Faculty of Engineering, Gifu University, 1-1 Yanagido, Gifu 501-1193, Japan; sano.hidetoshi.w4@f.gifu-u.ac.jp
[2] Center for Space Research and Utilization Promotion (c-SRUP), Gifu University, 1-1 Yanagido, Gifu 501-1193, Japan
[3] Department of Physics, Nagoya University, Furo-cho, Chikusa-ku, Nagoya 464-8601, Japan; yamane.y@a.phys.nagoya-u.ac.jp
[4] Lennard-Jones Laboratories, Keele University, Staffordshire ST5 5BG, UK; j.t.van.loon@keele.ac.uk
[5] National Astronomical Observatory of Japan, Mitaka, Tokyo 181-8588, Japan; kenji.furuya@nao.ac.jp
[6] Western Sydney University, Locked Bag 1797, Penrith South DC, NSW 1797, Australia
[7] Department of Physics, Graduate School of Science, The University of Tokyo, 7-3-1 Hongo, Bunkyo-ku, Tokyo 113-0033, Japan
[8] Research Center for the Early Universe, School of Science, The University of Tokyo, 7-3-1 Hongo, Bunkyo-ku, Tokyo 113-0033, Japan
[9] Trans-Scale Quantum Science Institute, The University of Tokyo, Tokyo 113-0033, Japan
[10] Department of Astronomy, University of Virginia, Charlottesville, VA 22904, USA
[11] National Radio Astronomy Observatory, 520 Edgemont Road, Charlottesville, VA 22903, USA
[12] Department of Physics, Konan University, 8-9-1 Okamoto, Higashinada, Kobe, Hyogo 6588501, Japan
[13] Astronomical Observatory Belgrade; Volgina 7, 11060 Belgrade, Serbia
[14] Center for Astrophysics | Harvard & Smithsonian, 60 Garden Street, Cambridge, MA 02138, USA
[15] Department of Physics, Graduate School of Science, Osaka Metropolitan University, 1-1 Gakuen-cho, Naka-ku, Sakai, Osaka 599-8531, Japan
[16] Department of Physics, University of Texas at Arlington, Box 19059, Arlington, TX 76019, USA
[17] SETI Institute, 189 N. Bernardo Avenue, Suite 200, Mountain View, CA 94043, USA
[18] JBCA, Department of Physics and Astronomy, University of Manchester, UK
[19] School of Physical Sciences, The University of Adelaide, North Terrace, Adelaide, SA 5005, Australia
[20] Dr. Karl Remeis-Sternwarte, Erlangen Centre for Astroparticle Physics, Friedrich-Alexander-Universität Erlangen-Nürnberg, Sternwartstraβe 7, D-96049 Bamberg, Germany
[21] Department of Physics and Astronomy, University of Missouri, Columbia, MO 65211, USA
[22] Key Laboratory of Optical Astronomy, National Astronomical Observatories, Chinese Academy of Sciences, Beijing 100012, People's Republic of China
[23] Leiden Observatory, Leiden University, P.O. Box 9513, NL-2300 RA Leiden, The Netherlands
[24] International Centre for Radio Astronomy Research (ICRAR), University of Western Australia, 35 Stirling Highway, Crawley, WA 6009, Australia
[25] ARC Centre of Excellence for All Sky Astrophysics in 3 Dimensions (ASTRO 3D), Australia
[26] Princeton University, 4 Ivy Lane, Princeton, NJ 08544, USA
[27] Department of Earth and Planetary Sciences, Faculty of Science, Kyushu University, Nishi-ku, Fukuoka 819-0395, Japan

Abstract

We present the first compelling evidence of shock-heated molecular clouds associated with the supernova remnant (SNR) N49 in the Large Magellanic Cloud (LMC). Using ^{12}CO($J = 2$–1, 3–2) and ^{13}CO($J = 2$–1) line emission data taken with the Atacama Large Millimeter/Submillimeter Array, we derived the H_2 number density and kinetic temperature of eight ^{13}CO-detected clouds using the large velocity gradient approximation at a resolution of $3\farcs5$ (~0.8 pc at the LMC distance). The physical properties of the clouds are divided into two categories: three of them near the shock front show the highest temperatures of ~50 K with densities of ~500–700 cm^{-3}, while other clouds slightly distant from the SNR have moderate temperatures of ~20 K with densities of ~800–1300 cm^{-3}. The former clouds were heated by supernova shocks, but the latter were dominantly affected by the cosmic-ray heating. These findings are consistent with the efficient production of X-ray recombining plasma in N49 due to thermal conduction between the cold clouds and hot plasma. We also find that the gas pressure is roughly constant except for the three shock-engulfed clouds inside or on the SNR shell, suggesting that almost no clouds have evaporated within the short SNR age of ~4800 yr. This result is compatible with the shock-interaction model with dense and clumpy clouds inside a low-density wind bubble.

1. Introduction

Supernova remnants (SNRs) have a significant influence on the interstellar medium (ISM) via supernova shocks, injection of heavy elements, and cosmic-ray acceleration. In particular, shock heating and compression of a gaseous medium play an essential role not only in the evolution of the ISM but also in regulating both star formation and the structural evolution of galaxies (e.g., Inutsuka et al. 2015; Körtgen et al. 2016). Several pioneering observations have shown evidence of shock-heated molecular clouds at dozens of kelvins in the vicinity of Galactic SNRs using the non-local thermodynamic

equilibrium (non-LTE) approximation (e.g., Cornett et al. 1977; White et al. 1987). Seta et al. (1998) presented enhanced ^{12}CO $J = 2–1/1–0$ intensity ratios of $\gtrsim 1–3$ in shocked molecular clouds in Galactic SNRs W44 and IC 443, and derived typical kinetic temperatures of $\sim 40–80$ K in these clouds. Subsequent molecular-line observations also established the presence of supernova-shocked warm clouds using non-LTE codes, and discussed their relation to star formation and/or high-energy phenomena (e.g., Reach & Rho 1999; Anderl et al. 2014; Rho et al. 2015, 2017; Hogge et al. 2019; Sano et al. 2021a, 2021b; Mazumdar et al. 2022). More recently, an unusually high HCO$^+$/CO ratio has also been observed in molecular clouds interacting with SNRs, possibly due to high cosmic-ray ionization rates (Zhou et al. 2022). On the other hand, there have been no such studies on extragalactic SNRs especially in the Large Magellanic Cloud (LMC), despite the advantages of very little contamination along the line of sight (a small inclination angle of the LMC disk $\sim 20°–30°$; e.g., Subramanian & Subramaniam 2010) and its known distance ($\sim 50 \pm 1.3$ kpc; Pietrzyński et al. 2013).

LHA 120-N49 (hereafter N49) in the LMC is one of the best extragalactic SNRs to study shock-heating and compression of a gaseous medium because it is believed to be associated with molecular clouds (e.g., Banas et al. 1997; van Loon et al. 2010a; Uchida et al. 2015). The bright radio shell of N49 with centrally filled thermal X-rays is a typical characteristic of a mixed-morphology SNR (Rho & Petre 1998). Although N49 has an apparent diameter of only $\sim 75''$ (or ~ 18.2 pc; see Bozzetto et al. 2017), Chandra resolved its filamentary diffuse emission and bright knots of X-rays at a resolution of $\sim 0''5$ (e.g., Park et al. 2003, 2012). The Sedov age of N49 was estimated to ~ 4800 yr (Park et al. 2012). The nearby star-forming activity and spectral characteristics of the SNR generally support a massive progenitor star for N49 (Klose et al. 2004; Badenes et al. 2009; Yamaguchi et al. 2014). The projection of the magnetar candidate SGR 0526$-$66 within the boundary of N49 may support a core-collapse origin for N49, although the physical association between N49 and SGR 0526 $-$66 is not conclusive (e.g., Gaensler et al. 2001; Park et al. 2012). Thus, while the Type Ia origin may not be completely ruled out based on the Si/S ejecta abundance ratio (e.g., Park et al. 2012), a core-collapse origin from the explosion of a massive progenitor is generally considered for N49.

A giant molecular cloud (GMC) in the N49 region was first discovered by Banas et al. (1997) using the ^{12}CO($J = 2–1$) emission line with the Swedish-ESO Submillimeter Telescope at a resolution of $\sim 23''$ or ~ 5.5 pc. The GMC has a diameter of ~ 14 pc and lies on the southeastern shell of N49, in the direction in which the SNR is brightest in both the radio continuum and X-rays. The authors concluded that the GMC is possibly associated with the SNR. Subsequent Mopra observations using the ^{12}CO($J = 1–0$) emission line also supported this idea (Sano et al. 2017a). An important breakthrough came from observations of the ^{12}CO($J = 1–0$) emission line by Yamane et al. 2018 (hereafter Paper I) using the Atacama Large Millimeter/Submillimeter Array (ALMA). Thanks to the high angular resolution of ALMA of $3''2 \times 2''3$ (or 0.78 pc$\times$ 0.56 pc), the GMC was resolved into 21 molecular clouds. At least three of them are limb-brightened on sub-parsec scales in both hard X-rays and radio continuum, suggesting shock–cloud interactions (e.g., Inoue et al. 2009; Sano et al. 2010; Inoue et al. 2012).

In this paper, we derive the H$_2$ number density and kinetic temperature of molecular clouds in the vicinity of the SNR N49 using ALMA observations of ^{12}CO($J = 1–0$, $2–1$, $3–2$) and ^{13}CO($J = 2–1$) and a non-LTE analysis. Our findings for the shock- and/or cosmic-ray-heated clouds provide a new perspective on the ISM surrounding extragalactic SNRs for the first time. In Section 2, we present the observational details and data reduction of the ALMA CO data as well as archival X-ray data. Section 3 gives an overview of CO distributions and their physical properties. In Sections 4 and 5 we discuss and summarize our findings.

2. Observations and Data Reduction

2.1. ALMA CO

We carried out observations of ^{12}CO($J = 3–2$) emission line using the ALMA Atacama Compact Array Band 7 in Cycle 8 (PI: Hidetoshi Sano, #2021.2.00008.S). We used 10–11 antennas of the 7 m array in 2022 August 22, 27, 30, and September 2. We also used 3–4 antennas of the Total Power (TP) array in 2022 August 2, 4, 7, 8, 13, 17, 18, 20, and 27. The effective observed area was an approximately $1'.2 \times 1'.3$ rectangular region centered at $(\alpha_{J2000}, \delta_{J2000}) = (05^h26^m04^s.82, -66°05'23''.8)$. The baseline range of the 7 m array was from 8.9 to 91.0 m, corresponding to $u–v$ distances from 10.2 to 105.0 $k\lambda$ at 345.796 GHz. Bandpass and flux calibration were carried out using quasar J0538$-$4405 and we used quasar J0601 $-$7036 as a phase calibrator.

Observations of ^{12}CO($J = 2–1$) and ^{13}CO($J = 2–1$) emission lines were carried out using ALMA Band 6 in Cycle 3 (PI: Jacco Th. van Loon, #2015.1.01195.S). We used 45–46 antennas of the 12 m array in 2016 January 27 and 28; 8–10 antennas of the 7 m array in 2016 August 30, 31, September 2 and 4. The effective observed area was an approximately $1' \times 1'$ rectangular region centered at $(\alpha_{J2000}, \delta_{J2000}) = (05^h26^m04^s.00, -66°05'20''.0)$. The combined baseline range of the 12 and 7 m arrays was from 8.9 to 331.0 m, corresponding to $u–v$ distances from 6.8 to 254.5 $k\lambda$ at 230.538 GHz. The bandpass calibration was carried out by observing three quasars J0519$-$4546, J0522$-$3627, and J0006 $-$0623. Another two quasars, J0529$-$7245 and J0601$-$7036, were observed as phase calibrators. We also used Uranus, J0538$-$4405, and J0601$-$7036 as flux calibrators.

Data reduction and imaging were performed using the Common Astronomy Software Applications package (CASA, version 5.4.1; CASA Team et al. 2022). We applied the multiscale CLEAN algorithm with the natural weighting scheme (Cornwell 2008). Here we used the `tclean` task to make the images. We then combined the cleaned 7 m data and the calibrated TP array data for CO($J = 3–2$) and the cleaned 12 and 7 m array data for CO($J = 2–1$) using the `feather` task. The final beam size of the feathered image was $3''.48 \times 2''.76$ with a position angle of $33°.7$ for the ^{12}CO($J = 3–2$) emission line; $1''.73 \times 1''.10$ with a position angle of $76°.7$ for the ^{12}CO($J = 2–1$) emission line; and $1''.82 \times 1''.14$ with a position angle of $77°.0$ for the ^{13}CO($J = 2–1$) emission line. The typical rms noise was ~ 0.11 K at a velocity resolution of 0.4 km s^{-1} for the ^{12}CO($J = 3–2$) emission line, and ~ 0.09 K at a velocity resolution of 0.4 km s^{-1} for both the ^{12}CO($J = 2–1$) and ^{13}CO($J = 2–1$) emission lines. The primary beam correction
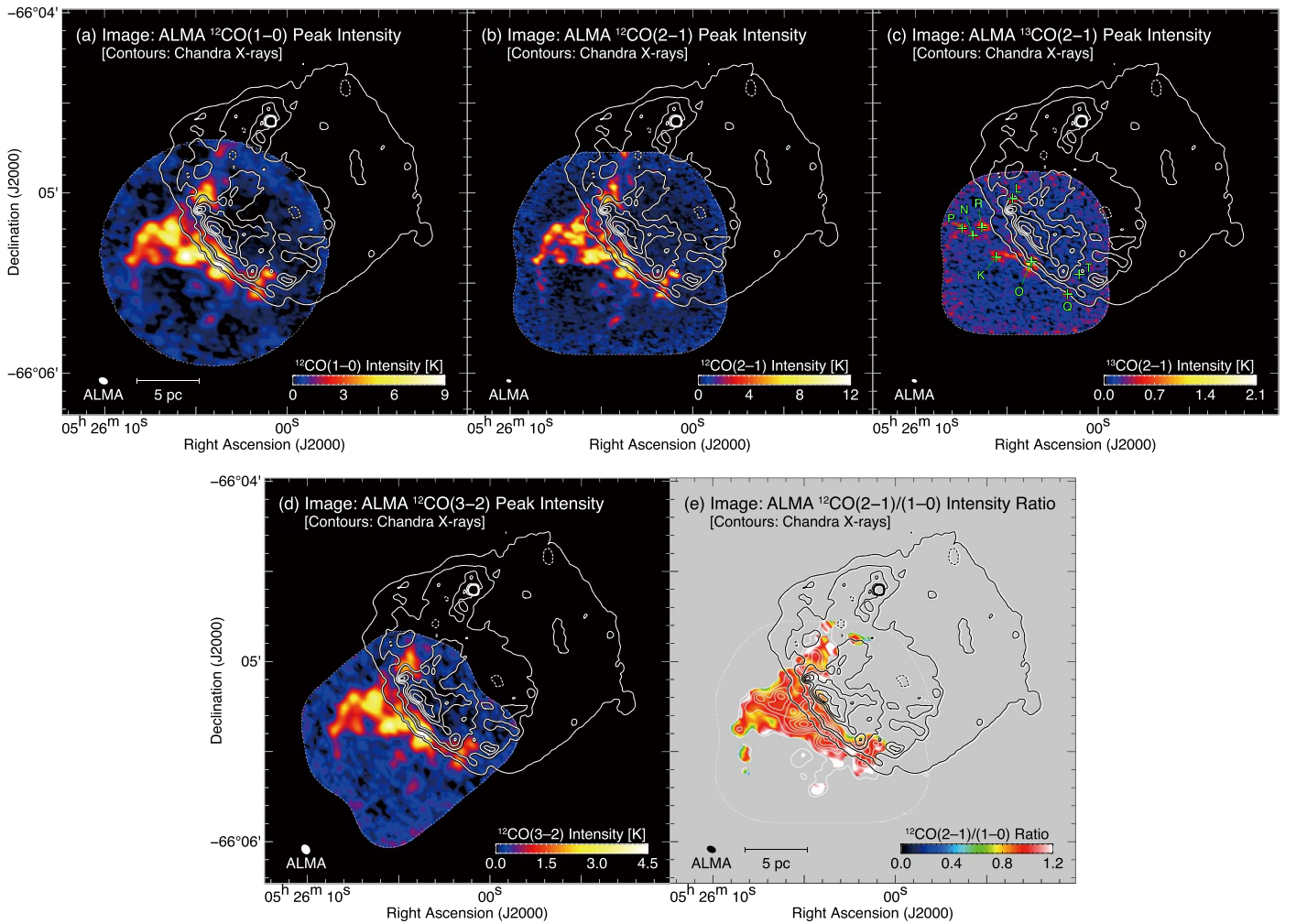
Figure 1. Peak intensity maps of (a) $^{12}\text{CO}(J=1\text{--}0)$, (b) $^{12}\text{CO}(J=2\text{--}1)$, (c) $^{13}\text{CO}(J=2\text{--}1)$, and (d) $^{12}\text{CO}(J=3\text{--}2)$. (e) Intensity ratio map of $^{12}\text{CO}(J=2\text{--}1)/^{12}\text{CO}$ $(J=1\text{--}0)$ (hereafter $R_{2\text{--}1/1\text{--}0}$). The velocity range of CO is from 285.5 to 287.8 km s^{-1}. Superposed contours represent Chandra X-ray intensity in the energy band of 0.5–7.0 keV. The lowest contour level and the contour intervals are 5×10^{-7} and 3×10^{-6} photons pixel^{-1} s^{-1}, respectively. The regions enclosed by dashed lines indicate the observed areas using ALMA. The CO peaks K, L, N, O–R, and T defined by Paper I are also indicated in (c). When we take the intensity ratio of $R_{2\text{--}1/1\text{--}0}$, the $^{12}\text{CO}(J=2\text{--}1)$ data were smoothed with a two-dimensional Gaussian kernel to match the effective beam size of the $^{12}\text{CO}(J=1\text{--}0)$ data. The gray shaded area in (e) represents the $^{12}\text{CO}(J=1\text{--}0)$ and/or $^{12}\text{CO}(J=2\text{--}1)$ data showing significance lower than $\sim 10\sigma$.

was applied with a threshold of 0.2 for $^{12}\text{CO}(J=2\text{--}1)$ and 0.5 for $^{12}\text{CO}(J=3\text{--}2)$ and $^{13}\text{CO}(J=2\text{--}1)$.

In order to take an intensity ratio of two different CO J-transitions, we also used the primary-beam-corrected, $^{12}\text{CO}(J=1\text{--}0)$ cleaned data published in Paper I. The beam size was $3\rlap{.}{''}19 \times 2\rlap{.}{''}25$ with a position angle of $66\rlap{.}{°}14$. The typical rms noise was ~ 0.07 K at a velocity resolution of 0.4 km s^{-1}.

2.2. Chandra X-Rays

We utilized archival X-ray data obtained by Chandra with the Advanced CCD Imaging Spectrometer S-array (ACIS-S3). The observation IDs were 747, 1041, 1957, 2515, 10123, 10806, 10807, and 10808, and were published in previous papers (Park et al. 2003, 2012, 2020; Paper I; Zhou et al. 2019). We utilized Chandra Interactive Analysis of Observations software (CIAO version 4.12; Fruscione et al. 2006) with CALDB 4.9.1 (Graessle et al. 2007) for the data reduction. All of the data were reprocessed using the task chandra_repro. The total effective exposure reached ~ 197 ks for the eastern rim of the SNR, where the shock–cloud interactions occur. We

then made an exposure-corrected, energy-filtered image using the task uximage in the energy band of 0.5–7.0 keV as a broadband X-ray image.

3. Results

3.1. Distributions of CO and X-Rays

Figures 1(a)–(d) show the peak intensity maps of $^{12}\text{CO}(J=1\text{--}0)$, $^{12}\text{CO}(J=2\text{--}1)$, $^{13}\text{CO}(J=2\text{--}1)$, and $^{12}\text{CO}(J=3\text{--}2)$ at $V_{\text{LSR}} = 285.5\text{--}287.8$ km s^{-1}, corresponding to the shocked components in N49 (Paper I). The clouds detected in $^{12}\text{CO}(J=2\text{--}1)$ and $^{12}\text{CO}(J=3\text{--}2)$ are situated along the southeastern edge of the X-ray shell and their spatial distribution is consistent with that seen in $^{12}\text{CO}(J=1\text{--}0)$ in Paper I.

In comparison to ^{12}CO, the ^{13}CO clouds are distributed more sparsely (see Figure 1(c)). Generally, in the LMC, both pre-star formation and active star-forming clouds exhibit relatively similar distributions for ^{12}CO and ^{13}CO (e.g., Wong et al. 2019), often forming prominent filamentary structures (e.g., Fukui et al. 2019; Tokuda et al. 2019). The compact, peculiar nature of the ^{13}CO distribution in N49 is distinct from the above-mentioned interstellar trends, and unique to this SNR.

Table 1
Physical Properties of ^{13}CO Detected Clouds in SNR N49

Name	α_{J2000}	δ_{J2000}	T_b			V_{peak}	$\triangle V$	Size	M_{vir}	R_{dist}	T_{kin}	$n(H_2)$
			^{12}CO(3–2)	^{12}CO(2–1)	^{13}CO(2–1)							
	(h m s)	(° ′ ″)	(K)	(K)	(K)	(km s^{-1})	(km s^{-1})	(pc)	($M_\odot$)	(pc)	(K)	(10^3 cm^{-3})
(1)	(2)	(3)	(4)	(5)	(6)	(7)	(8)	(9)	(10)	(11)	(12)	(13)
K	5:26:5.5	−66:05:21	3.60	6.59	0.35	285.5	0.83	1.3	80	10.7	45^{+14}_{-9}	$0.53^{+0.05}_{-0.06}$
L	5:26:4.7	−66:05:02	2.00	3.75	0.18	286.3	1.72	1.2	340	7.7	42^{+26}_{-13}	$0.72^{+0.13}_{-0.14}$
N	5:26:6.7	−66:05:15	2.58	4.67	0.40	286.4	0.40	0.8	10	11.6	21^{+4}_{-3}	$0.78^{+0.02}_{-0.04}$
O	5:26:3.7	−66:05:23	4.91	8.26	0.91	286.2	0.69	1.2	50	8.8	19^{+1}_{-2}	$1.10^{+0.01}_{-0.01}$
P	5:26:7.5	−66:05:12	2.17	3.70	0.36	286.4	1.00	1.1	100	12.2	19^{+4}_{-3}	$1.32^{+0.01}_{-0.03}$
Q	5:26:1.7	−66:05:34	1.82	3.64	0.25	286.5	0.90	1.0	80	9.6	21^{+6}_{-4}	$0.81^{+0.06}_{-0.05}$
R	5:26:6.3	−66:05:11	3.17	5.49	0.51	286.4	0.86	1.1	80	10.7	20^{+3}_{-2}	$1.10^{+0.02}_{-0.03}$
T	5:26:1.0	−66:05:27	1.55	2.94	0.14	286.4	0.57	0.9	30	7.7	46^{+57}_{-18}	$0.48^{+0.09}_{-0.14}$

Notes. Column (1): Cloud name defined by Paper I. Columns (2, 3): Position of the maximum intensity of ^{12}CO($J = 1$–0) (Paper I). Columns (4–8): Physical properties of CO emission derived from a single Gaussian fitting. All the CO data sets were smoothed to match the beam size of $3''.5 \times 3''.5$. Columns (4–6): Peak brightness temperature of ^{12}CO($J = 3$–2), ^{12}CO($J = 2$–1), and ^{13}CO($J = 2$–1) emission. Column (7): Central velocity of ^{13}CO($J = 2$–1) spectra, V_{peak}. Column (8): Full-width at half-maximum (FWHM) line width of ^{13}CO($J = 2$–1) spectra, $\triangle V$. Column (9): ^{13}CO($J = 2$–1) derived cloud size defined as $(A/\pi)^{0.5} \times 2$, where A is the total cloud surface area surrounded by the half intensity of peak integrated intensity contour. Column (10): Mass of the cloud derived using the virial theorem and ^{13}CO($J = 2$–1) properties, M_{vir}. Column (11): Radial distance from the geometric center of the SNR at $(\alpha_{J2000}, \delta_{J2000}) = (5^h25^m59^s.57, -66°04'56''.4)$. Column (12): Kinetic temperature, T_{kin}. Column (12): Number density of molecular hydrogen, $n(H_2)$.

Eight of them, K, L, N, O–R, and T, are detected in ^{13}CO($J = 2$–1) with 3σ or higher significance. The fundamental physical properties of ^{13}CO-detected clouds (position, brightness temperature, center velocity, spectral linewidth, cloud size, virial mass) are summarized in Table 1. In the present paper, we focus on these clouds to estimate their kinetic temperature and H$_2$ number density.

3.2. Intensity Ratio of ^{12}CO(J = 2–1)/^{12}CO(J = 1–0)

Figure 1(e) shows the intensity ratio distribution of ^{12}CO($J = 2$–1)/^{12}CO($J = 1$–0) (hereafter $R_{2-1/1-0}$). The intensity ratio is a good indicator of the degree of the CO rotational excitation because the $J = 2$ level is at an excitation energy of $E/k = 16.5$ K, $\sim$10 K above the $J = 1$ level at $E/k = 5.5$ K (e.g., Seta et al. 1998). We find a high intensity ratio of $R_{2-1/1-0} \sim 1.0$–1.2 in the entire molecular cloud associated with the SNR. We also confirmed that the intensity ratio distribution of ^{12}CO($J = 3$–2)/^{12}CO($J = 1$–0) is similar to that of $R_{2-1/1-0}$. It is noteworthy that no extra heating sources such as OB stars and/or young stellar objects are associated with the molecular clouds in the vicinity of the SNR.

3.3. Large Velocity Gradient Analysis

In order to estimate the kinetic temperature T_{kin} and H$_2$ number density $n(H_2)$ of molecular clouds in N49, we performed a non-LTE analysis using the large velocity gradient (LVG) approximation (e.g., Goldreich & Kwan 1974; Scoville & Solomon 1974). This non-LTE code calculates the radiative transfer of multiple transitions of atomic and/or molecular lines, assuming an isothermal spherical cloud with uniform photon escape probability and velocity gradient of dv/dr. Here, dv is the half-maximum half-width (HMHW) linewidth of the CO line profile derived by least-squares fitting with a Gaussian kernel, and dr is the cloud radius. Since the eight molecular clouds have different cloud sizes and linewidths, we calculated individual dv/dr for each cloud. We also used the abundance ratio of [^{12}CO/H$_2$]=1.6×10^{-5} and the abundance ratio of isotopes [^{12}CO/^{13}CO]$= 50$ (e.g., Blake et al. 1987;

Mizuno et al. 2010; Minamidani et al. 2011; Fujii et al. 2014). The ^{12}CO($J = 1$–0) data were not included in the LVG analysis because the lowest-J transition may be subject to self-absorption owing to a large optical depth (e.g., Mizuno et al. 2010).

Figure 2 shows the typical LVG results, T_{kin}–$n(H_2)$ relation, and CO spectra for clouds P, R, and L. The post-shocked cloud L on the shock front shows higher kinetic temperature T_{kin} $\sim$42 K and relatively lower H$_2$ number density $n(H_2)$ $\sim$720 cm^{-3}, while the ambient cloud P away from the SNR shell shows lower $T_{kin} \sim$19 K and moderate $n(H_2) \sim$1320 cm^{-3}. The pre-shocked cloud R lying between them shows similar values of T_{kin} and $n(H_2)$ to the ambient cloud P ($T_{kin} \sim$20 K and $n(H_2) \sim$1100 cm^{-3}). This trend is also found in other molecular clouds in N49. It is noteworthy that clouds K, L, and T show lower ^{13}CO($J = 2$–1)/^{12}CO($J = 3$–2) ratios than other clouds.

Figure 3 shows the radial distributions of X-ray intensity and T_{kin} of the eight molecular clouds from the geometric center of the SNR at $(\alpha_{J2000}, \delta_{J2000}) = (05^h25^m59^s.57, -66°04'56''.4)$. To calculate the shell diameter and thickness of the X-ray shell in N49, we performed a least-squares fitting using a three-dimensional spherical shell model with a Gaussian function $F(r)$ (e.g., Sano et al. 2017b, 2021a; Aruga et al. 2022):

$$F(r) = A \exp[-(r - r_0)^2/2\sigma^2], \qquad (1)$$

where A is the normalization factor of the Gaussian function, r_0 is the shell radius, r is the radial distance from the geometric center of the SNR, and σ is the standard deviation of the Gaussian function. We obtained a shell radius of 7.7 ± 1.8 pc and shell thickness of 2.6 ± 4.5 pc as the best-fit parameters of the fitting, where the shell thickness was defined as the FWHM of the Gaussian function.

Figure 4 shows the scatter plot between T_{kin} and $n(H_2)$ for the eight molecular clouds. Clouds N, O, P, Q, and R show a negative correlation which was fitted by the least-squares method using the MPFITEXY routine (Williams et al. 2010), while T_{kin} of clouds K, L, and T seems to be shifted to higher values compared to the other molecular clouds.
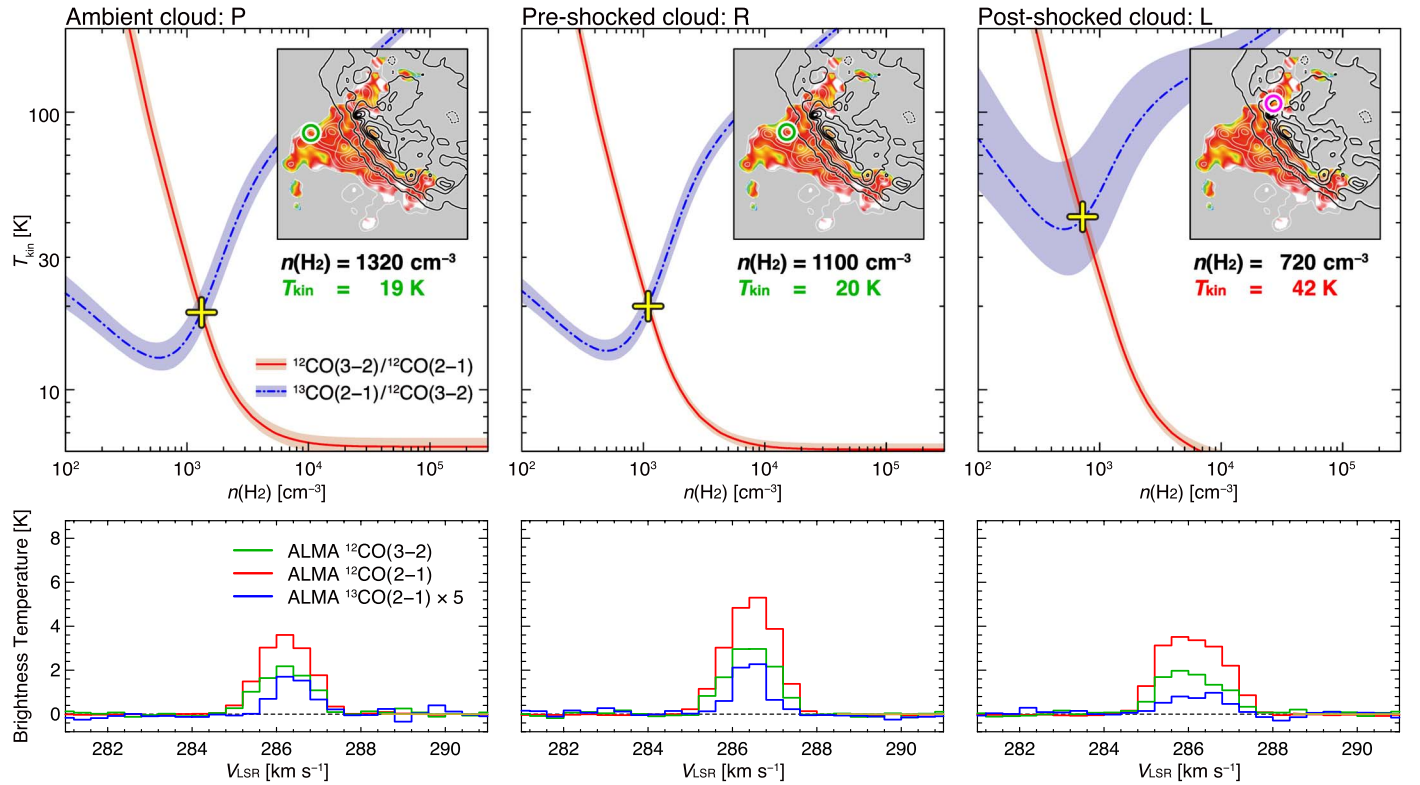
Figure 2. Top panels: large velocity gradient results on the number density of molecular hydrogen, $n(H_2)$, and the kinetic temperature, T_{kin}, for the ambient cloud P, pre-shocked cloud R, and the post-shocked cloud L. The red lines and blue dashed-dotted lines indicate the intensity ratios of $^{12}CO(J = 3\text{–}2)/^{12}CO(J = 2\text{–}1)$ and ^{13}CO $(J = 2\text{–}1)/^{12}CO(J = 3\text{–}2)$, respectively. The shaded areas surrounding the red and blue lines indicate the 1σ ranges of each intensity ratio. Yellow crosses represent the best-fit values of $n(H_2)$ and T_{kin} for each cloud. The spatial positions and best-fit values for each cloud are shown in the top-right corners for each panel. Bottom panels: CO intensity profiles for clouds P, R, and L. The physical properties of each cloud are summarized in Table 1.

4. Discussion

The observed spatial variation in T_{kin} and $n(H_2)$ of the molecular clouds associated with N49 has many implications for the evolution of the supernova-shocked ISM. First, we argue that the high temperatures of ∼40–50 K as seen in clouds K, L, and T are likely caused by shock-heating. According to Paper I, these clouds are tightly interacting with shockwaves and enhance the turbulent magnetic field with bright synchrotron radiation on the surface of the shocked clouds, suggesting that clouds K, L, and T are located inside the SNR or on the shock front. Quantifying this scenario requires a decomposition of the density and velocity distribution of clouds K, L, and T which requires even higher-resolution data (e.g., Menon et al. 2021; Sharda et al. 2022). Although clouds O, Q, and R have smaller radial distances than cloud K, this is likely due to projection effects. In addition, the observed cloud temperatures are roughly consistent with those measured in shock-heated molecular clouds associated with several Galactic SNRs (e.g., Seta et al. 1998; Sano et al. 2021a, 2021b). The lack of local excitation sources other than SNR shocks also supports this scenario. If so, this is the first compelling evidence of "shock-heated" molecular clouds associated with an extragalactic SNR.

The shock-heating scenario is also consistent with the thermal conduction origin of the recombining plasma (RP) discovered in N49 (Uchida et al. 2015). The RP is characterized by a higher ionization temperature compared to the electron temperature, which is not expected in the classical evolution model of thermal plasma in SNRs (see also the review by Yamaguchi 2020). To achieve the RP state, rapid electron cooling or an increase of the ionization state is needed.

One of the possible scenarios is the rapid cooling of electrons via thermal conduction between the shocks and cold/dense clouds (e.g., Kawasaki et al. 2002; Matsumura et al. 2017a, 2017b; Okon et al. 2018, 2020; Sano et al. 2021b). Paper I found that the hard-band X-rays due to radiative recombination are enhanced around the shocked clouds including clouds K, L, and T. The authors concluded that the RP in N49 was efficiently produced by shocked CO clouds due to thermal conduction, which is consistent with the higher kinetic temperatures of clouds K, L, and T. Additional spatially resolved X-ray spectroscopy with high-angular/spectral resolution is needed to confirm this scenario. The Athena mission has the potential to accomplish these (e.g., Nandra et al. 2013). It is noteworthy that the moderate dust temperature in cold components ∼20–30 K (pre-shocked dust) and in warm components ∼60 K (post-shocked dust) in N49 is also roughly consistent with our CO results (e.g., Otsuka et al. 2010; van Loon et al. 2010b; Lakićević et al. 2015), but the detailed comparison between the dust and CO clouds is beyond the scope of this paper.

Next, we argue that the moderate kinetic temperatures of ∼20 K seen in the other clouds N, O, P, Q, and R are likely due to cosmic-ray heating. According to Gabici et al. (2009), the diffusion length of cosmic rays l_{diff} in units of centimeters can be described as

$$l_{diff} = \sqrt{4D(E, B)t_{age}}, \qquad (2)$$

where $D(E, B)$ is the diffusion coefficient in units of $cm^2 \, s^{-1}$ and t_{age} is the SNR age in units of seconds. $D(E, B)$ can be written using the accelerated cosmic-ray energy E and the
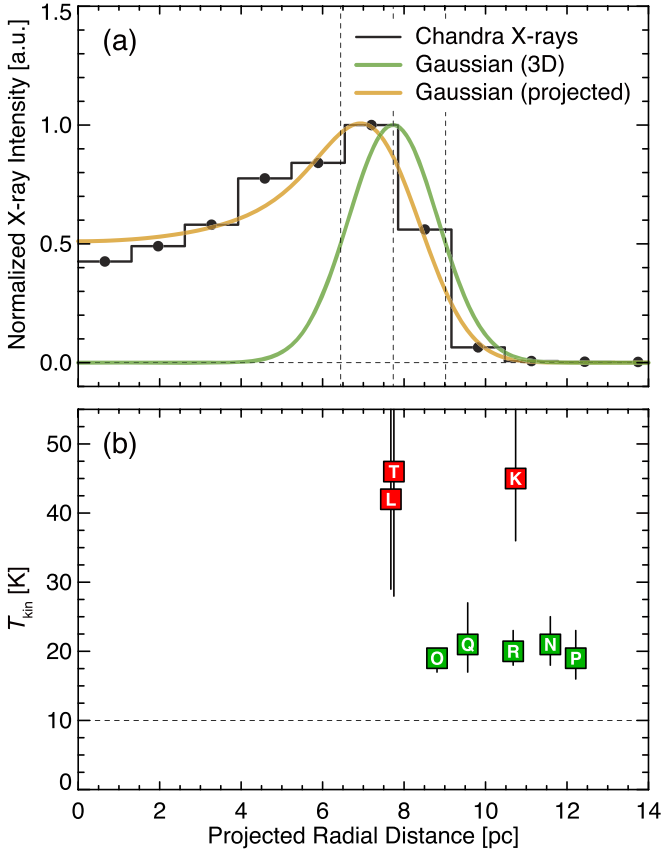
Figure 3. (a) Radial profile of the normalized X-ray intensity, centered at $(\alpha_{J2000}, \delta_{J2000}) = (05^h25^m59\overset{s}{.}57, -66°04'56\overset{s}{.}4)$ as the geometric center of the SNR. The steps with filled circles indicate averaged values of normalized X-ray intensity at each annulus. The green line indicates the three-dimensional Gaussian distribution, and the orange line represents its projected distribution given by the least-squares fitting (see the text). (b) Scatter plot of kinetic temperature T_{kin} for each cloud as a function of the projected radial distance. The dashed horizontal line represents $T_{kin}=10$ K, corresponding to the typical temperature of quiescent molecular clouds. The red and green symbols represent high- and moderate-temperature clouds, respectively.

magnetic field strength B as

$$D(E, B) = 5 \times 10^{26}\left(\frac{E}{100\text{ MeV}}\right)^{0.5}\left(\frac{B}{10\ \mu\text{G}}\right)^{-0.5}. \qquad (3)$$

Adopting $t_{age} = 1.5 \times 10^{11}$ s ($\sim$4800 yr; Park et al. 2012), $E = 100$ MeV, and $B = 10\ \mu$ G, we obtain $l_{diff} \sim 6$ pc which is substantially larger than the maximum separation between cloud P and the shock boundary of the SNR. This indicates that almost all cosmic ray particles accelerated in N49 have reached the entire region of the associated molecular clouds, and hence the cosmic-ray heating works equally well for both the post-shocked and pre-shocked clouds as well as the ambient clouds. In other words, cosmic-ray heating is not sufficient to increase the kinetic temperature of K, L, and T significantly above those of the unshocked clouds (O, Q, R, etc.).

We also argue that the moderate temperatures of the cosmic-ray-irradiated clouds are naturally explained by the high cosmic-ray ionization rates surrounding the SNR. Figure 5 shows the time evolution of the kinematic temperature T_{kin} at the cloud center after the supernova event that generated the LMC SNR N49, which was calculated as a function of cosmic-ray ionization rates ζ using a photodissociation region (PDR) model
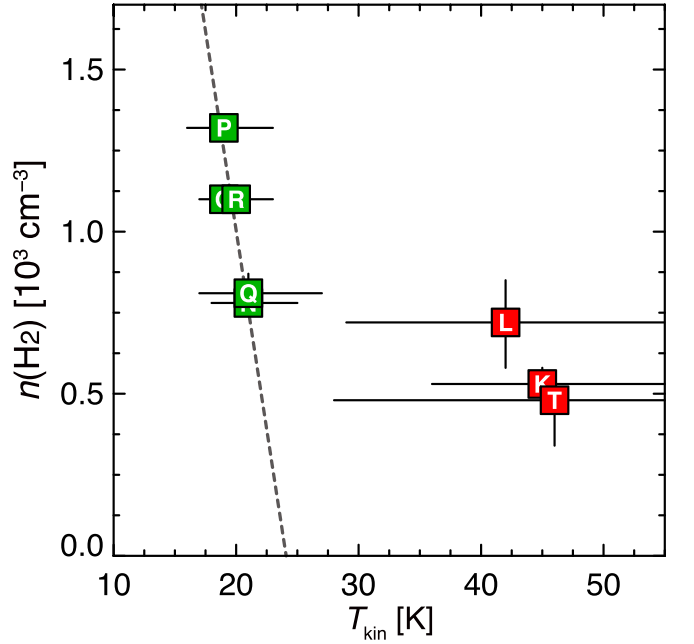
Figure 4. Scatter plot between T_{kin} and $n(H_2)$. The dashed line indicates the linear regression using the least-squares method except for the CO clouds L, K, and T (see the text).
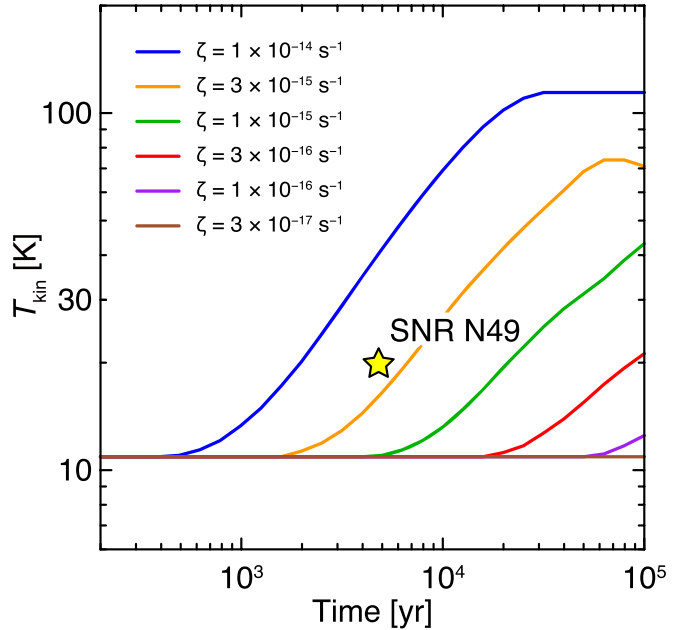
Figure 5. Time evolution of kinematic temperature T_{kin} at the cloud center after the supernova event that generates SNR N49. Colors indicate the assumed cosmic-ray ionization rate ζ from 3×10^{-17} s^{-1} to 1×10^{-14} s^{-1}. The star symbol indicates the observed values of T_{kin} for the ambient or pre-shocked clouds at the age of N49 (4800 yr).

(Furuya et al. 2022; see the Appendix for further details). Since the typical cosmic-ray ionization rates in the vicinity of Galactic SNRs are $\sim$30–300 times higher than the standard Galactic value of $\sim 10^{-17}$ s^{-1} (e.g., Indriolo et al. 2010; Ceccarelli et al. 2011; Vaupré et al. 2014), the observed values of $T_{kin} \sim 20$ K at pre-shocked and ambient clouds can be explained as the cosmic-ray heating effect. Further follow-up observations using multiple emission lines such as HCO$^+$, DCO$^+$ (e.g., Vaupré et al. 2014), and/or [CI] (Yamagishi et al. 2023) are needed to

estimate the cosmic-ray ionization rate in the vicinity of the LMC SNR N49.

Another interesting point is that these clouds, when exposed to a large number of cosmic rays, likely emit gamma-rays and X-ray line emission. Recent Fermi-LAT analysis of N49 presented a possible detection of hadronic gamma-rays which were produced by proton–proton interactions (Campana et al. 2022). The Fe Kα line emission at 6.4 keV was also discovered in several Galactic/Magellanic SNRs, which was probably produced by interactions between low-energy cosmic-ray protons and neutral irons in the ISM clouds (e.g., Bamba et al. 2009, 2018; Nobukawa et al. 2018, 2019; Okon et al. 2018). Further gamma-ray and X-ray observations at the high spatial and spectral resolutions using the Cherenkov Telescope Array (Actis et al. 2011; Cherenkov Telescope Array Consortium et al. 2019), the XRISM mission (Tashiro et al. 2020), and the Athena mission (Nandra et al. 2013) will allow us to unveil the high-energy radiation processes in N49.

Finally, we focus on possible cloud evaporation and/or destruction via shock–cloud interactions. In general, it is often assumed that interstellar gaseous clouds are immediately evaporated by supernova shocks in SNRs (e.g., Slavin et al. 2017; Wang et al. 2018; Zhang et al. 2019). However, this is correct only if the gas density contrast between the cloud and the inter-cloud gas densities is small, typically $\sim$100 or less. The initial ISM conditions before a core-collapse supernova explosion are expected to have a large density fluctuation of $\sim 10^5$ due to strong stellar winds from a massive progenitor. The low-density inter-cloud medium, such as atomic H I gas, was completely swept up by the winds over $\sim 10^6$ yr and then created a wind bubble with an interior density of ~ 0.01 cm^{-3} (Weaver et al. 1977). On the other hand, molecular clouds can survive wind erosion owing to their high densities, greater than $\sim 10^3$ cm^{-3}. When the shocks encounter the molecular cloud, the shock velocity V_{sh} dramatically decelerates to $V_{sh}/(n_{cloud}/n_0)^{0.5}$, where n_{cloud} is the cloud density and n_0 is the inter-cloud (ambient) density (see Section 39.3 in Draine 2011). Adopting the density contrast $n_{cloud}/n_0 = 10^5$, $V_{sh} = 3000$ km s^{-1}, and a cloud radius of 1 pc, the cloud-crossing time of supernova shocks is $\sim 10^5$ yr, and hence the cloud can survive the shock destruction within the typical lifetime of a SNR (see also a review by Sano & Fukui 2021).

We argue that the scenario can be applied to the SNR N49. The wind-bubble explosion scenario is consistent with the core-collapse origin of N49 (Gaensler et al. 2001; Klose et al. 2004; Badenes et al. 2009; Yamaguchi et al. 2014). The shocked molecular clouds are thought to have survived the erosion because we detect them using CO emission lines. Moreover, the negative correlation between T_{kin} and $n(H_2)$ indicates that clouds N, O, P, Q, and R have constant pressure and thus did not undergo shock evaporation. The enhanced magnetic field via shock–cloud interactions may also suppress thermal conduction and hamper cloud evaporation (e.g., Orlando et al. 2008). Interestingly, clouds K, L, and T located inside or on the edge of the SNR shell are significantly shifted from this pressure-constant line to a higher-pressure region and have slightly reduced number densities $n(H_2)$. This trend suggests that the clouds completely engulfed by shocks were partially evaporated through shock–cloud interactions. A similar trend is also seen in the shock-engulfed star-forming dense core C embedded within the Galactic SNR RX J1713.7−3946. Sano et al. (2010) presented a slightly steeper density gradient than

the typical star-forming cloud core, suggesting that only the surface of the cloud has been stripped out and heated up. In any case, the molecular clouds engulfed by the fast shocks in N49 were shown to decrease in number density rather than increase.

5. Summary

We summarize our conclusions as follows.

1. New ^{12}CO($J = 3$–2, 2–1) and ^{13}CO($J = 2$–1) observations using ALMA have revealed clumpy distributions of molecular clouds associated with SNR N49 in the LMC at a resolution of $1\rlap{.}''73 \times 1\rlap{.}''10$ or ~ 0.3 pc. The clouds completely delineate the southeastern edge of the SNR shell and show a high-intensity ratio of ^{12}CO($J = 2$–1)/^{12}CO($J = 1$–0) ~ 1.0–1.2, suggesting that shock–cloud interactions have occurred.

2. We applied a non-LTE LVG analysis toward the eight molecular clouds that are detected in ^{13}CO($J = 2$–1) emission with 3σ or higher significance. The kinetic temperature T_{kin} and number density of molecular hydrogen $n(H_2)$ of the post-shocked clouds located inside or on the shock front differed significantly from the other pre-shocked or ambient clouds; the cloud near the shock front shows the highest $T_{kin} \sim 50$ K and the lowest $n(H_2)$ ~ 0.5–0.7 $\times 10^3$ cm^{-3}, while the cloud ~ 5 pc away from the edge of the SNR has the lowest $T_{kin} \sim 20$ K and the densest $n(H_2)$ $\sim 1.3 \times 10^3$ cm^{-3}. Since the spatial variation of T_{kin} cannot be explained by cosmic-ray heating alone or extra heating sources like O-type stars, we conclude that the high T_{kin} values of the clouds were caused by supernova shocks. This is the first compelling evidence of shock-heated molecular clouds in an extragalactic SNR.

3. The negative correlation between T_{kin} and $n(H_2)$ indicates that clouds N, O, P, Q, and R have constant pressure and did not experience shock evaporation within the short SNR age of ~ 4800 yr. On the other hand, clouds K, L, and T, which are on the inside or on the edge of the shell, are significantly shifted from this pressure-constant line to a higher-pressure region and have slightly reduced densities, suggesting that the shock-engulfed clouds were partially evaporated through the shock–cloud interaction. The decreased density and increased pressure (and kinetic temperature) of the shocked molecular clouds have important implications for understanding the negative feedback of energetic supernova shocks on star formation. Further follow-up studies are needed from both the observational and theoretical sides.

Appendix
Time Evolution of the Kinetic Temperature

To estimate the impact of the cosmic-ray heating on the kinetic temperature, we run one-dimensional plane parallel PDR models (Furuya et al. 2022), which solve the time evolution of the gas temperature and abundances of chemical species self-consistently for given gas density distribution and dust-temperature distribution, considering gas-phase and gas–grain interaction (i.e., adsorption and desorption) and heating and cooling processes. Elemental abundances are taken from Acharyya & Herbst (2015; low metal abundances for the LMC in their Table 1). At the initial chemical state, we assume all hydrogen is in H_2, all carbon is in CO, and the remaining oxygen is in H_2O ice. The other elements are assumed to exist as either atoms or atomic ions in the gas phase.

The model simulation consists of two steps. In the first step, the model simulates the temporal evolution of the gas temperature and chemical abundances for 10^7 yr, assuming the standard ζ value of 1×10^{-17} s^{-1}. The chosen timescale of 10^7 yr is arbitrary, but it is long enough for the C^+, C^0, and CO abundances to reach steady-state values. In the second step, the model follows the evolution for 1×10^5 yr with an enhanced ζ value in a range between 3×10^{-17} s^{-1} and 1×10^{-14} s^{-1}. The first and second steps mimic conditions just before and after the supernova explosion, respectively. As input parameters for the model, we employ the UV intensity $G_0 = 110$ (Seok et al. 2012) and the hydrogen ($HI + H_2$) gas density $n_{HI + H_2} = 1 \times 10^3$ cm^{-3}. The dust temperature is calculated as a function of A_V using Equation (8) in Hocuk et al. (2017). The ratio of the hydrogen column density to A_V is assumed to be 3.5×10^{21} cm^{-2} (Cox et al. 2006). The gas temperature evolution at the cloud center ($A_V = 5$ mag.) after the explosion is shown in Figure 5.

ORCID iDs

H. Sano https://orcid.org/0000-0003-2062-5692
Y. Yamane https://orcid.org/0000-0001-8296-7482
J. Th. van Loon https://orcid.org/0000-0002-1272-3017
K. Furuya https://orcid.org/0000-0002-2026-8157
Y. Fukui https://orcid.org/0000-0002-8966-9856
R. Z. E. Alsaberi https://orcid.org/0000-0001-5609-7372
A. Bamba https://orcid.org/0000-0003-0890-4920
R. Enokiya https://orcid.org/0000-0003-2735-3239
M. D. Filipović https://orcid.org/0000-0002-4990-9288
R. Indebetouw https://orcid.org/0000-0002-4663-6827
T. Inoue https://orcid.org/0000-0002-7935-8771
A. Kawamura https://orcid.org/0000-0001-7813-0380
M. Lakićević https://orcid.org/0000-0002-8231-0963
C. J. Law https://orcid.org/0000-0003-1413-1776
T. Murase https://orcid.org/0000-0002-9552-3570
T. Onishi https://orcid.org/0000-0001-7826-3837
S. Park https://orcid.org/0000-0003-3900-7739
P. P. Plucinsky https://orcid.org/0000-0003-1415-5823
J. Rho https://orcid.org/0000-0003-3643-839X
A. M. S. Richards https://orcid.org/0000-0002-3880-2450
G. Rowell https://orcid.org/0000-0002-9516-1581
M. Sasaki https://orcid.org/0000-0001-5302-1866
J. Seok https://orcid.org/0000-0002-0070-3246
P. Sharda https://orcid.org/0000-0003-3347-7094
L. Staveley-Smith https://orcid.org/0000-0002-8057-0294
H. Suzuki https://orcid.org/0000-0002-8152-6172
T. Temim https://orcid.org/0000-0001-7380-3144
K. Tokuda https://orcid.org/0000-0002-2062-1600
K. Tsuge https://orcid.org/0000-0002-2794-4840
K. Tachihara https://orcid.org/0000-0002-1411-5410

References

Acharyya, K., & Herbst, E. 2015, ApJ, 812, 142
Actis, M., Agnetta, G., Aharonian, F., et al. 2011, ExA, 32, 193
Anderl, S., Gusdorf, A., & Güsten, R. 2014, A&A, 569, A81
Aruga, M., Sano, H., Fukui, Y., et al. 2022, ApJ, 938, 94
Badenes, C., Harris, J., Zaritsky, D., & Prieto, J. L. 2009, ApJ, 700, 727
Bamba, A., Ohira, Y., Yamazaki, R., et al. 2018, ApJ, 854, 71
Bamba, A., Yamazaki, R., Kohri, K., et al. 2009, ApJ, 691, 1854
Banas, K. R., Hughes, J. P., Bronfman, L., & Nyman, L. Å. 1997, ApJ, 480, 607
Blake, G. A., Sutton, E. C., Masson, C. R., & Phillips, T. G. 1987, ApJ, 315, 621
Bozzetto, L. M., Filipović, M. D., Vukotić, B., et al. 2017, ApJS, 230, 2
Campana, R., Massaro, E., Bocchino, F., et al. 2022, MNRAS, 515, 1676
CASA Team, Bean, B., Bhatnagar, S., et al. 2022, PASP, 134, 114501
Cherenkov Telescope Array Consortium, Acharya, B. S., Agudo, I., et al. 2019, Science with the Cherenkov Telescope Array (Singapore: World Scientific)
Ceccarelli, C., Hily-Blant, P., Montmerle, T., et al. 2011, ApJL, 740, L4
Cornett, R. H., Chin, G., & Knapp, G. R. 1977, A&A, 54, 889
Cornwell, T. J. 2008, ISTSP, 2, 793
Cox, N. L. J., Cordiner, M. A., Cami, J., et al. 2006, A&A, 447, 991
Draine, B. T. 2011, Physics of the Interstellar and Intergalactic Medium (Princeton, NJ: Princeton Univ. Press)
Fruscione, A., McDowell, J. C., Allen, G. E., et al. 2006, Proc. SPIE, 6270, 62701V
Fujii, K., Minamidani, T., Mizuno, N., et al. 2014, ApJ, 796, 123
Fukui, Y., Tokuda, K., Saigo, K., et al. 2019, ApJ, 886, 14
Furuya, K., Tsukagoshi, T., Qi, C., et al. 2022, ApJ, 926, 148
Gabici, S., Aharonian, F. A., & Casanova, S. 2009, MNRAS, 396, 1629
Gaensler, B. M., Slane, P. O., Gotthelf, E. V., & Vasisht, G. 2001, ApJ, 559, 963
Goldreich, P., & Kwan, J. 1974, ApJ, 189, 441
Graessle, D. E., Evans, I. N., Glotfelty, K., et al. 2007, ChNew, 14, 33
Hocuk, S., Szűcs, L., Caselli, P., et al. 2017, A&A, 604, A58
Hogge, T. G., Jackson, J. M., Allingham, D., et al. 2019, ApJ, 887, 79
Indriolo, N., Blake, G. A., Goto, M., et al. 2010, ApJ, 724, 1357
Inoue, T., Yamazaki, R., Inutsuka, S.-i., et al. 2009, ApJ, 695, 825
Inoue, T., Yamazaki, R., Inutsuka, S.-i., & Fukui, Y. 2012, ApJ, 744, 71
Inutsuka, S.-i., Inoue, T., Iwasaki, K., & Hosokawa, T. 2015, A&A, 580, A49
Kawasaki, M. T., Ozaki, M., Nagase, F., et al. 2002, ApJ, 572, 897
Klose, S., Henden, A. A., Geppert, U., et al. 2004, ApJL, 609, L13

Körtgen, B., Seifried, D., Banerjee, R., Vázquez-Semadeni, E., & Zamora-Avilés, M. 2016, MNRAS, 459, 3460

Lakićević, M., van Loon, J. T., Meixner, M., et al. 2015, ApJ, 799, 50

Landsman, W. B. 1993, in ASP Conf. Ser. 52, Astronomical Data Analysis Software and Systems II, ed. R. J. Hanisch, R. J. V. Brissenden, & J. Barnes (San Francisco, CA: ASP), 246

Matsumura, H., Tanaka, T., Uchida, H., Okon, H., & Tsuru, T. G. 2017a, ApJ, 851, 73

Matsumura, H., Uchida, H., Tanaka, T., et al. 2017b, PASJ, 69, 30

Mazumdar, P., Tram, L. N., Wyrowski, F., Menten, K. M., & Tang, X. 2022, A&A, 668, A180

Menon, S. H., Federrath, C., Klaassen, P., Kuiper, R., & Reiter, M. 2021, MNRAS, 500, 1721

Minamidani, T., Tanaka, T., Mizuno, Y., et al. 2011, AJ, 141, 73

Mizuno, Y., Kawamura, A., Onishi, T., et al. 2010, PASJ, 62, 51

Nandra, K., Barret, D., Barcons, X., et al. 2013, arXiv:1306.2307

Nobukawa, K. K., Hirayama, A., Shimaguchi, A., et al. 2019, PASJ, 71, 115

Nobukawa, K. K., Nobukawa, M., Koyama, K., et al. 2018, ApJ, 854, 87

Okon, H., Tanaka, T., Uchida, H., et al. 2020, ApJ, 890, 62

Okon, H., Uchida, H., Tanaka, T., Matsumura, H., & Tsuru, T. G. 2018, PASJ, 70, 35

Orlando, S., Bocchino, F., Reale, F., Peres, G., & Pagano, P. 2008, ApJ, 678, 274

Otsuka, M., van Loon, J. T., Long, K. S., et al. 2010, A&A, 518, L139

Park, S., Bhalerao, J., Kargaltsev, O., & Slane, P. O. 2020, ApJ, 894, 17

Park, S., Burrows, D. N., Garmire, G. P., et al. 2003, ApJ, 586, 210

Park, S., Hughes, J. P., Slane, P. O., et al. 2012, ApJ, 748, 117

Pietrzyński, G., Graczyk, D., Gieren, W., et al. 2013, Natur, 495, 76

Reach, W. T., & Rho, J. 1999, ApJ, 511, 836

Rho, J., Hewitt, J. W., Bieging, J., et al. 2017, ApJ, 834, 12

Rho, J., Hewitt, J. W., Boogert, A., Kaufman, M., & Gusdorf, A. 2015, ApJ, 812, 44

Rho, J., & Petre, R. 1998, ApJL, 503, L167

Sano, H., Fujii, K., Yamane, Y., et al. 2017a, in AIP Conf. Proc. 1792, 6th Int. Symp. on High Energy Gamma-Ray Astronomy (Melville, NY: AIP), 040038

Sano, H., & Fukui, Y. 2021, Ap&SS, 366, 58

Sano, H., Sato, J., Horachi, H., et al. 2010, ApJ, 724, 59

Sano, H., Suzuki, H., Nobukawa, K. K., et al. 2021a, ApJ, 923, 15

Sano, H., Yamane, Y., Voisin, F., et al. 2017b, ApJ, 843, 61

Sano, H., Yoshiike, S., Yamane, Y., et al. 2021b, ApJ, 919, 123

Sault, R. J., Teuben, P. J., & Wright, M. C. H. 1995, in ASP Conf. Ser. 77, Astronomical Data Analysis Software and Systems IV, ed. R. A. Shaw, H. E. Payne, & J. J. E. Hayes (San Francisco, CA: ASP), 433

Scoville, N. Z., & Solomon, P. M. 1974, ApJL, 187, L67

Seok, J. Y., Koo, B.-C., & Onaka, T. 2012, ApJ, 744, 160

Seta, M., Hasegawa, T., Dame, T. M., et al. 1998, ApJ, 505, 286

Sharda, P., Menon, S. H., Federrath, C., et al. 2022, MNRAS, 509, 2180

Slavin, J. D., Smith, R. K., Foster, A., et al. 2017, ApJ, 846, 77

Subramanian, S., & Subramaniam, A. 2010, A&A, 520, A24

Tashiro, M., Maejima, H., Toda, K., et al. 2020, Proc. SPIE, 11444, 1144422

Tokuda, K., Fukui, Y., Harada, R., et al. 2019, ApJ, 886, 15

Uchida, H., Koyama, K., & Yamaguchi, H. 2015, ApJ, 808, 77

van Loon, J. T., Oliveira, J. M., Gordon, K. D., et al. 2010a, AJ, 139, 68

van Loon, J. T., Oliveira, J. M., Gordon, K. D., Sloan, G. C., & Engelbracht, C. W. 2010b, AJ, 139, 1553

Vaupré, S., Hily-Blant, P., Ceccarelli, C., et al. 2014, A&A, 568, A50

Wang, Y., Bao, B., Yang, C., & Zhang, L. 2018, MNRAS, 478, 2948

Weaver, R., McCray, R., Castor, J., Shapiro, P., & Moore, R. 1977, ApJ, 218, 377

White, G. J., Rainey, R., Hayashi, S. S., & Kaifu, N. 1987, A&A, 173, 337

Williams, M. J., Bureau, M., & Cappellari, M. 2010, MNRAS, 409, 1330

Wong, T., Hughes, A., Tokuda, K., et al. 2019, ApJ, 885, 50

Yamagishi, M., Furuya, K., Sano, H., et al. 2023, PASJ, 75, 883

Yamaguchi, H. 2020, AN, 341, 150

Yamaguchi, H., Badenes, C., Petre, R., et al. 2014, ApJL, 785, L27

Yamane, Y., Sano, H., van Loon, J. T., et al. 2018, ApJ, 863, 55

Zhang, G.-Y., Slavin, J. D., Foster, A., et al. 2019, ApJ, 875, 81

Zhou, P., Vink, J., Safi-Harb, S., & Miceli, M. 2019, A&A, 629, A51

Zhou, P., Zhang, G.-Y., Zhou, X., et al. 2022, ApJ, 931, 144